Published in final edited form as:
J Am Chem Soc. 2007 March 21; 129(11): 3135–3147.

Intermediates in dioxygen activation by methane monooxygenase: A QM/MM study

David Rinaldo[†], **Dean M. Philipp**[‡], **Stephen J. Lippard**[*,§], and **Richard A. Friesner**[*,†]
Contribution from the Departments of Chemistry and Center for Biomolecular simulation, Columbia University, New York, New York 10027, Schrodinger Inc, 101 SW Main Street, Portland, OR 97204, Massachusetts Institute of Technology, Cambridge, Massachusetts 02139

Abstract

Protein effects in the activation of dioxygen by methane monooxygenase (MMO) were investigated by using combined QM/MM and broken-symmetry Density Functional Theory (DFT) methods. The effects of a novel empirical scheme recently developed by our group on the relative DFT energies of the various intermediates in the catalytic cycle are investigated. Inclusion of the protein leads to much better agreement between the experimental and computed geometric structures for the reduced form ($MMOH_{red}$). Analysis of the electronic structure of $MMOH_{red}$ reveals that the two iron atoms have distinct environments. Different coordination geometries tested for the $MMOH_{peroxo}$ intermediate reveal that, in the protein environment, the μ-η^2,η^2 structure is more stable than the others. Our analysis also shows that the protein helps to drive reactants towards products along the reaction path. Furthermore, these results demonstrate the importance of including the protein environment in our models and the usefulness of the QM/MM approach for accurate modeling of enzymatic reactions. A discrepancy remains in our calculation of the Fe-Fe distance in our model of H_Q as compared to EXAFS data obtained several years ago, for which we currently do not have an explanation.

Keywords

Soluble Methane Monooxygenase; Methylococcus-capsulatus Bath; Nonheme Diiron Enzymes; Dinuclear Iron Centers; DFT; Density Functional Theory; Catalytic Cycle; Dioxygen Activation; O Bond-Cleavage; Intermediate Q; Peroxide Intermediate

Introduction

Soluble methane monooxygenase (sMMO) is a multicomponent enzyme complex that catalyzes the oxidation of methane to methanol in methanotrophic bacteria such as *Methylococcus capsulatus* (Bath) and *Methylosinus trichosporium* OB3b (Scheme 1):[1–8]

The complex is at present believed to involve a minimum of three components. The hydroxylase (MMOH) catalyzes the oxidation reaction at a non-heme, carboxylate bridged dinuclear iron center held within a four-helix bundle. The reductase component (MMOR) is a flavin- and ferredoxin-containing protein that transfers electrons from NADH to reduce the diiron center of MMOH to its Fe(II)-Fe(II) state. Component B is a cofactorless protein required

---

[*] To whom correspondence should be adressed. E-mail: rich@chem.columbia.edu, lippard@mit.edu.
[†] Columbia University.
[‡] Schrödinger Inc.
[§] Massachusetts Institute of Technology.

for efficient catalysis that also serves several regulatory roles. A fourth component, MMOD, has recently been characterized. Its function is still unclear, but it binds to MMOH and is a potent inhibitor of sMMO. It has been proposed to play a role in the assembly of the MMOH diiron center.[9]

An important reason for the attention devoted to sMMO is its ability to oxidize the C-H bond of methane selectively to methanol under ambient temperature and pressure conditions. The understanding of the mechanism by which the enzyme catalyzes this chemically challenging reaction would not only be of great academic interest but also of possible practical value for the biomimetic design of new catalysts for the industrial conversion of methane to methanol.[10–12] Substantial advances in the understanding of this mechanism at an atomic level have been accomplished these last years through structural and spectroscopic studies[1, 3, 6–8] as well as computational investigations.[13–18]

The catalytic cycle of sMMO can formally be divided into two steps: dioxygen activation and substrate oxidation (Figure 1). O_2 activation can occur once the diiron center in the resting, oxidized form $\mathrm{MMOH_{ox}}$ is reduced by MMOR to form $\mathrm{MMOH_{red}}$. Then, diffusion of O_2 to the hydroxylase active site leads to the formation of $\mathrm{MMOH_{superoxo}}$, which has an Fe(II)-Fe(III)(O_2^-) iron core.[19] Subsequently, $\mathrm{MMOH_{superoxo}}$ converts to the diamagnetic peroxo compound ($\mathrm{MMOH_{peroxo}}$), the first intermediate spectroscopically characterized in the cycle after O_2 reacts with $\mathrm{MMOH_{red}}$.[8, 20–25] Based on comparisons with synthetic model compounds, cis-μ-1,2 peroxo, μ-η^1-η^1 or end-on structures were suggested[26–29] for $\mathrm{MMOH_{peroxo}}$, whereas a μ-η^2-η^2 butterfly structure has been proposed based on results from DFT studies.[16, 19] The last step in dioxygen activation yields intermediate Q ($\mathrm{MMOH_Q}$). This compound harbors two high-valent, antiferromagnetically-coupled, Fe(IV)-Fe(IV) atoms in nearly equivalent environments.[20, 21, 30, 31] A $\mathrm{Fe(IV)_2}$-$(\mu\text{-O})_2$ diamond core with a short Fe-Fe distance has been proposed for this intermediate based on an EXAFS study.[31] This intermediate reacts to convert methane into methanol yielding $\mathrm{MMOH_{ox}}$.[21, 23, 25, 32] The final steps of the mechanism, in which a hydrogen is abstracted from substrate, followed by recombination of the substrate with the resulting OH moiety in the core to produce hydroxylated product (methanol, in the case of a methane substrate) have been discussed extensively in previous work.[5, 8, 14, 33–40] In ref. [42], this reaction is modeled using quantum dynamical methods, and both concerted and “radical rebound” mechanisms (the latter involving a very short lived bound radical species) are shown to contribute to the reaction pathway. We shall not discuss substrate oxidation further in the present paper, which is focused on dioxygen activation.

Extensive theoretical studies of dioxygen activation have been carried out in our group[13, 14, 19, 41, 42] and others.[43–48] Those studies were based on model clusters of different sizes, using mainly Density Functional Theory (DFT). Calculations using large (~100 atom) models suggest that the protein plays a significant role in dioxygen activation, and that a more rigorous analysis of the protein contributions to the activation process would be useful. To date, the only quantum mechanics/molecular mechanics (QM/MM) calculations have focused on the study of $\mathrm{MMOH_{ox}}$ and $\mathrm{MMOH_{red}}$ using the ONIOM method[49, 50] and on the hydroxylation of several substrates by $\mathrm{MMOH_Q}$ using the frozen orbital methodology.[39]

The aim of the present paper is to analyze the structural and energetic effects of the protein on the different intermediates of the dioxygen activation pathway in the sMMO catalytic cycle. After describing the model and the methodology used for this study, the results obtained will be presented. They will be subsequently discussed in light of experimental data to gain insight into dioxygen activation mechanism and the role the protein matrix could play. To conclude, our results will be summarized.

Methods

Computational Methods

QM/MM methods—Over the past decade, we have developed the QM/MM program QSite[51] based on a frozen orbital approach.[52–54] This program results from a tight coupling between Jaguar[55] and the protein modeling program IMPACT[56, 57] developed by Levy and coworkers. The OPLS-AA[58, 59] molecular mechanics force field is used for the treatment of the MM part while the pure QM part was treated at the DFT-B3LYP level of theory, with details as discussed in the next section.

The methodology has been extensively tested and shown to give reliable results for the relative conformational energies of dipeptides[52–54] and protonation energies of protein side-chains.[52, 53] Moreover, it has successfully been applied to a number of biological systems[13] such as the studies of the MMO hydroxylation step,[39] P450,[60, 61] hemerythrin,[62] triosephosphate isomerase (TIM),[63] class C β-lactamase and Penicillin binding protein (PBP).[39] The errors resulting from the QM/MM interface are quite small in an absolute sense (~0.5 kcal/mol) and are expected to be unimportant as compared to intrinsic errors in the DFT methodology.[52, 53]

The antiferromagnetic coupling of the two iron atoms of intermediates in the catalytic cycle requires the use of unrestricted DFT (UDFT) methods to obtain reliable models. Until now this feature was not implemented into QSite and we therefore had to resort to a thermodynamic cycle, presented in Supporting Information, to get proper energetics. In the present study, the QM/MM//UDFT scheme recently implemented into QSite[64] has been used; the results obtained are compared to those generated using the previous scheme. The good agreement generally obtained between the two approaches validates the thermodynamic cycle used in our previous QM/MM studies.[62, 65]

QM methods—The core computational method chosen for this study is density functional theory (DFT)[66] with the hybrid functional B3LYP.[67–69] An unrestricted DFT (UDFT) methodology was employed to model spin polarization efficiently for open shell orbitals of both irons. This method enables modeling of antiferromagnetic (AF) coupling between the two Fe atoms by the use of a broken symmetry (BS) wave function. The Jaguar[55] suite of *ab initio* quantum chemical programs was used for all standalone QM calculations. This program using pseudospectral methods is particularly efficient for treating large size systems such as those found in biology[70, 71] and its high-quality initial-guess wavefunctions for metals are very useful for studying bioinorganic systems.[72, 73]

The choice of the basis set is also an important issue in computational studies. Our previous studies have shown that geometry optimizations using a mixed basis set, such as LACVP**[74–76] for metals, 6-31G* on core atoms and 6-31G on the remaining atoms, gives reasonable results. For this study we used LACVP** for metals and 6-31G* on other atoms for consistency with QM/MM calculation, since frozen orbitals are only available with the 6-31G* basis set. Accurate energy determinations require single point calculations with larger basis sets of triple-ζ quality in the diiron core, such as the scheme we have previously used with LACV3P** on metals, cc-pVTZ(-f)[77] on core atoms and 6-31G** otherwise. We also add diffuse functions (cc-pVTZ(-f)++) onto both atoms of dioxygen because these atoms are strongly negatively charged in $\mathrm{MMOH_Q}$. The results shown below indicate that the enhancement of the basis set on the core oxygen atoms yields improved results for the relative energetics of the various intermediates in the catalytic cycle.

Vibrational frequency calculations are highly computationally demanding tasks for big models. It is therefore necessary to use smaller models with lower quality basis sets for this purpose.

In the present work, the LACVP**/6-31G** basis set was used for the core atoms and 6-31G was used otherwise.

Finally, we have recently developed a novel scheme for correcting errors in DFT energetics based on localized orbital corrections (LOC).[78] When applied to a data set of 222 molecules containing first and second row atoms for which accurate enthalpies of formation, ionization potentials, electron affinities or proton affinities are experimentally well known (G3 dataset[79]), the mean absolute deviation (MAD) versus experiment for the B3LYP version of the methodology (B3LYP-LOC) is 0.8 kcal/mol, as compared to the MAD of 4.8 kcal/mol obtained for B3LYP alone. The methodology at present has only been robustly optimized and tested for first and second row atoms, but we can make a simple extension to apply it to the relative energetics of the various species involved in the MMOH catalytic cycle. We investigate the effects of these corrections for intermediates in MMO dioxygen activation. Although more work is required to achieve quantitatively accurate parametrization for transition metals, the localized corrections in their current form appear to provide significantly improved results for the relative energetics of the $MMOH_Q$ and $MMOH_{peroxo}$ states, as revealed by comparisons to experimental data.

Physical Model

Our QM/MM models are based on the QM/MM structure of $MMOH_Q$ built in our previous study;[65] this structure in turn was initially derived starting from the crystal structure of the oxidized form.[80, 81] Due to the fact that the QM/MM code QSite[64] was only able to handle at most 8000 atoms, and in order to restrict computational effort, only residues and water molecules within 35 Å of the active site of an α subunit of the $\alpha_2\beta_2\gamma_2$ MMOH were included in our calculations (Figure 2). To mimic solvent screening, all surface residues not engaged in salt bridges were neutralized. The QM region includes Glu 114, Glu144, His 147, Glu 209, Glu 243, His 246, a water molecule, and the diiron core, including dioxygen- or solvent-derived ligands when present. Backbone cuts were performed for both His 147 and His 246, whereas side chain cuts were used for the other residues. It should be noted that in our previous calculations, side chain cuts were also used for both histidines. However, our QM/MM//RDFT calculations revealed that important forces are exerted on the frozen bonds of the histidines. Such important forces on the QM/MM boundaries might generate artifacts in the energy. Although these errors should cancel by the use of the thermodynamic cycle in QM/MM//RDFT calculations, they may be more important in the QM/MM//UDFT scheme.

For the final system, the QM part and the whole QM/MM model were both neutral. The initial guess geometries of each intermediate were setup by modifying the diiron core and, when needed, Glu 243 in our model of $MMOH_Q$ to match better the geometries of the pure QM models obtained in our previous study.[19] This task was performed by using the program Maestro,[83] superimposing the QM cluster onto the $MMOH_Q$, changing distances and angles for the diiron core, and only modifying dihedral angles for Glu 243.

Pure QM calculations were carried out by taking the QM regions obtained in the QM/MM calculations, cutting the models between the C_α and the C_β, and then capping the dangling bonds with hydrogen atoms. Frequency calculations were performed on medium-sized models (~50 atoms) derived from the QM/MM//RDFT structures, modeling glutamates by acetates and histidines by imidazoles. All zero point energies (ZPE) and thermochemical corrections were derived from these calculations performed after optimization of the capping hydrogen atoms and without frequency scaling.

Results

Geometries and electronic structures of reaction cycle compounds

In this section, we analyze, for each compound of the catalytic reaction cycle, the geometry and electronic structure obtained to characterize the effect of the protein matrix and to determine the state of the species we are proposing.

Reduced form—The reduced form was modeled with two ferromagnetically coupled, high spin (S=2) iron(II) atoms in agreement with experimental evidence[21, 84–86] and previous theoretical results.[19] After QM/MM optimization, the structure obtained gives RMSDs for heavy atoms of the diiron cluster and the liganded side chains of 0.35 Å and 0.33 Å, respectively, with the crystal structures[87] of the two protomers (the RMSD between the protomers' crystal structures is 0.15 Å). The QM/MM model for the reduced structure of the enzyme is in very good agreement with experiment (Figure 3). This result contrasts with the pure QM calculation using a large cluster model, for which a RMSD of 0.99 Å was found for almost the same heavy atoms as in the QM/MM for RMSD calculation.

The distance between Fe(II) ions reflects dramatically improved agreement between the QM/MM and the experimental structures. In our calculation, a distance of 3.29 Å was found between iron atoms, comparable to the experimental distance of 3.27–3.31 Å (Table 1). In contrast, in the pure QM calculation, the distance was 3.64 Å, clearly beyond the range of experimental and theoretical errors, as noted in our previous papers.[19, 41] The distances between the iron and coordinated atom of the various protein and solvent-derived ligands are qualitatively similar in both the QM/MM and the pure QM models when compared to experiment. However, a more quantitative examination of the results reveals the deviation of selected distances between the QM/MM models and the crystallographic structure to be close to the deviation observed between the two crystallographic protomers, whereas the deviation obtained with the QM model was almost twice as large (Table 1). A closer analysis shows that the poorer RMSD obtained with the QM model is mainly due to contributions from the bridging water molecule O14 (Figure 3) and to the oxygen O11 from Glu 243. It is also interesting to note that the structural agreement of the QM/MM model is better with protomer β than with protomer α (data not shown), and that this discrepancy is also due to O11 (Glu 243), O13 (axial water) and O14 (bridging water). Moreover, in protomer α, the water molecule O14 (Figure 3) is hydrogen bonded to both Glu 209 and to another water molecule located 2.96 Å away, whereas in protomer β the second water is farther away in the pocket (4.90 Å), precluding formation of a hydrogen bond with O14. In our QM/MM models the second water is not included. Thus, the choice of our model, structurally closer to protomer β, could explain its deviation from protomer α. These results also show that the geometry of the reduced state, and particularly the distances between iron ions and water molecules, are strongly dependent on the solvent hydrogen-bonding network, supporting the proposal that this network could play an important role during the reduction of $MMOH_{ox}$.[44, 45] To test this hypothesis, we have built a new model including, in the MM region, the two water molecules present in the crystal structure of protomer α. The results obtained (data not shown) improved the agreement with the first-shell distances of protomer α (MAD of 0.142 Å) as well as the distance between Fe1 and O14. Interestingly, in presence of the new water molecules, Glu 209 and Fe2 are displaced whereas the other ligands are minimally perturbed (Figure 4). This effect is consistent with the proposed reduction mechanism,[45] and is also in good agreement with the fact that Fe2 is more labile than Fe1 in the reduced state.[87]

The QM/MM model shows that the protein matrix is responsible for the short Fe-Fe distance in the reduced state. Indeed, all previous QM models have consistently computed a substantially larger iron-iron distance than those found experimentally, and including second sphere ligands or electrostatic effects of the protein and solvent in a continuum model, did not entirely solve this problem.[19, 41, 44, 50] To understand the origin of the short Fe-Fe distance found in the current study, we analyze our data and determine the forces acting on the various atoms of our QM/MM//RDFT model. The calculations of forces were carried out in vacuum and with point charges in place of MM atoms to distinguish electrostatic from strain effects of the protein. Forces acting on residues were obtained by summing up forces acting on all atoms of each residue.

The results are presented in Table 2/Figure 5 and show that strain forces (arrows in black on the right) and, to a lesser extent total forces (yellow arrows on the left), tend to keep residues of the active site grouped around the iron ions and to compress the active site. This property is particularly true for residues Glu 114, His 147, Glu 209 and His 246. The case of Glu 243 is different, because the protein tends to move it away from the diiron core. This result is consistent with the fact that, in the oxidized form, this ligand is rotated and no longer bonded to both Fe1 and Fe2. The origin of protein forces tending to keep the active site of the reduced form compact and thus driving the large decrease in the iron-iron distance is probably the four-helix bundle fold. Analysis shows that interactions leading to the contraction of the active site occur between helices B-C on one hand and E-F on the other hand (Figure 5 and Table 2). But it must be noted that, even if these interactions can at least partly explain the decreased Fe-Fe distance, interactions in the orthogonal direction (i.e. B–E and C–F) would be more efficient since they would be collinear with the iron-iron vector.

Forces exerted by the protein on each atom (data not shown) show very important forces of opposite directions on $N\varepsilon_2$ and $H\varepsilon_2$ of both histidines. This result is probably due to the well-conserved aspartates (Asp 143, Asp 242), hydrogen bonded to histidines, that attract Hε2 while the protein backbone tends to keep Nε2 atoms in place. This observation emphasizes the role of Asp 143 and Asp 242 as noted in our previous paper, and which were included in our cluster models therein.[41]

To determine the energy the protein has to expend to keep the iron atoms at a shorter distance than in the QM models, we carried out a QM optimization of the capped QM region of our QM/MM model, first constraining the positions of the iron ions and then allowing a full optimization. The results show that constraining the iron-iron distance at the value of our QM/MM model has a cost of 9.7 kcal/mol. The difference between the QM and QM/MM models is therefore not due to a flat potential energy surface along the iron-iron coordinate. Rather, the protein matrix effect is important energetically and the protein has to expand significant energy to keep the iron-iron distance at the experimentally observed value.

The electronic structure analysis of our model shows that there are 8 unoccupied low-energy beta-spin orbitals that are mainly centered on the iron ions. The beta-spin HOMO and HOMO-1 are also centered on Fe1 and Fe2 respectively (see detailed analysis in Supporting Information). Thus, the electronic structure of H_{red} is consistent with two high-spin ferrous iron atoms. But, despite their common oxidation state, the electronic structure reveals that the two iron atoms are not equivalent. Indeed, the two iron atoms are in different environments (Figure 6), with Fe1 having an octahedral geometry and Fe2 being in a square pyramidal environment.

Reduced form without coordinated water (H_{red}-no-wat)—Geometry optimization of the reduced form of the enzyme, after departure of the loosely coordinated water molecule trans to the histidines (O14), yields a QM/MM structure similar to that of the original reduced enzyme model; the RMSD between them (without O14) is only 0.12 Å (Figure S-3). Differences are mainly due to a slight increase in the Fe-Fe distance from 3.29 Å to 3.38 Å, to a slight shift of Glu 243 so that the single-atom bridge between the two iron atoms is more effective, and to an important shift of the axial water on Fe1 (O13) due to an increase of the angle with His 147 (O13-Fe1-N_{His147}) from 92° to 102°. This similarity is also reflected at the electronic level; the same electronic configuration as in the reduced state is found for the iron cations. Since the electronic structure of the iron atoms is not affected by the water departure, the water is only bound to iron cations through electrostatic interactions. Given the fact that these iron atoms are in a relatively low oxidation state, and are surrounded by negatively charged ligands, the weak coordination of the water molecule can be rationalized. The departure of the water is also correlated with an increased Fe-Fe distance, probably because the water molecule helps to reduce electrostatic repulsion between the iron atoms, allowing them to stay closer in the pure reduced form.

Attack of dioxygen: formation of the superoxo intermediate—The first step in dioxygen activation is formation of $H_{superoxo}$. This electron transfer process, which involves different spin coupling schemes and different geometries, has been extensively studied in our previous paper.[19] We basically follow the lowest energy path that was found therein: binding of dioxygen to form the undecet $H_{superoxo}$ (S=5), then intersystem crossings (ISC) to yield $H_{superoxo}$ in its triplet state (S=1) and then in its singlet state (S=0).

The structure of $H_{superoxo}$ (S=5) obtained at the QM/MM level is slightly different from the one obtained via pure QM calculations;[19] an RMSD between the two structures of 0.83 Å is obtained for the active site atoms. This RMSD is primarily due to differences located on the ligands of Fe2, because Glu 243 and dioxygen are less tilted toward Fe2, in a way similar to what was found in our earlier study[41] (with which it has a RMSD of 0.72 Å), and His 246 does not rotate as in the pure QM calculation. The Fe-Fe distance of 3.44 Å is shorter than in our pure QM models (3.79 Å in [[19]] and 3.71 Å in [[41]]) therefore showing that the protein matrix tends also to decrease the Fe-Fe distance in the $H_{superoxo}$ (S=5) state. Analysis (see Supporting Information) shows that this state has an electronic structure intermediate between those of H_{red} complexed with O_2 and a true $H_{superoxo}$ form, since no π^* orbital of O_2 is fully filled. Similar electronic structures with intermediate characters have already been pointed out in metal-dioxygen complexes.[88]

The QM/MM structure of the triplet (S=1) $H_{superoxo}$ is very similar to the one obtained for the undecet (S=5) state (RMSD of 0.10 Å). Electronic structure analysis (see Supporting Information) shows that the electron transfer occurs in this triplet state because the charge-transfer from Fe2 to dioxygen is much more important than in the undecet state. Thus, the electronic structure is consistent with a state mixing in approximately equal amounts those of a pure reduced enzyme state (no electron transfer to dioxygen) and a pure superoxo state (one electron transferred to dioxygen).

The structure of the singlet is closer to the structure of the undecet (RMSD of 0.04 Å) than the one of the triplet (0.08 Å). The electronic structure of this state of $H_{superoxo}$ is compatible with a true superoxide species with the electron transferred to the dioxygen molecule coming from Fe2. This is consistent with the fact that dioxygen preferentially binds Fe2, and thus electron transfer from Fe2 is facilitated. It can therefore be noticed that, for this species, Fe2 appears to be less electrophilic than Fe1 while in a previous study[89] on MMO_Q (*vide infra*) the reverse was observed. This is actually not inconsistent, because the iron atoms in these species are in different oxidation states and moreover, we have shown (*vide supra*) that in the reduced state the iron atoms experience different ligand fields. It is therefore difficult to predict the electrophilicity of Fe1 and Fe2 without taking into account the particular state of the catalytic cycle in question.

The peroxide intermediate—The next step involves a second electron transfer from Fe1 to the dioxygen molecule to yield a peroxide intermediate. We have previously proposed two possible structures for this intermediate based on pure QM calculations.[19, 41] We investigated both models with QM/MM, but also reconsidered two additional structures. All these possibilities are presented in Figure 7. It was previously shown,[19] after extensive QM investigations, that for an ~100 atom model, the lowest energy structure was the μ-η^2,η^2 butterfly arrangement in its singlet state. However, we investigated again all four alternatives at the QM/MM level to see whether the protein could change their relative energies. Moreover, we also investigated the possibility of a cis-μ-1,2 coordination of peroxide to the iron atoms since it has been recently shown that this coordination geometry was favored in a ribonucleotide reductase variant.[90]

The QM/MM μ-η^2,η^2 butterfly structure displays a noticeable similarity to its pure QM counterpart (in both the undecet and singlet states); the RMSD between them is only 0.59 Å for both states. The Fe1-Fe2 distance in the QM/MM model (3.48 Å) is smaller than that in the undecet and singlet QM models (3.64 Å and 3.61 Å respectively, Table 3 and Table S-3), and the value of the dihedral angle Fe1-O1-O2-Fe2 (defined in Figure 8) is 144.8°.

The μ-η^2,η^1 (also called asymmetric APER[19]) structure proposed for H_{peroxo} is very similar structurally to the analogous geometry proposed for $H_{superoxo}$. The main differences observed are:

- a more pronounced shift of Glu 243 in the peroxo species so that the oxygen bridges both irons more symmetrically.
- a slight shift of dioxygen closer to both iron atoms and mainly toward Fe1.

The QM/MM structure obtained here is slightly different from the pure QM model previously obtained (RMSD of 0.77 Å). The protein modestly decreases the iron-iron distance from 3.36 Å to 3.27 Å. The dihedral angle involving the peroxide moiety and the iron centers is 102.6°.

Two structures were tested for the cis-μ-1,2 H_{peroxo} species. One (Aμ-1,2 H_{peroxo}) was based on the μ-η^2,η^1 H_{peroxo} (asymmetric structure: Aperoxo) and the other (Sμ-1,2 H_{peroxo}) on the μ-η^2,η^2 butterfly structure (Speroxo) (Figure 7). The QM/MM structure of Sμ-1,2 H_{peroxo} is very similar to that of the μ-η^2,η^2 butterfly H_{peroxo} species with distances of 1.87 Å between the closer oxygen atom of the peroxo moiety and both Fe1 and Fe2. The Fe-Fe distance increases from 3.48 Å in the μ-η^2,η^2 structure to 3.64 Å in the Sμ-1,2H_{peroxo} structure. This increase is relatively large compared to those for the other species and is probably due to the lack of a single-atom bridge between the iron atoms and the subsequent increased electrostatic repulsion between the two cations. This effect is more marked in the full QM calculation for which the Fe-Fe distance reaches 4.02 Å in the Sμ-1,2 structure compared to 3.61 Å for μ-η^2,η^2 H_{peroxo} (Table 3). These results again emphasize the role of the protein, which tends to reduce the Fe-Fe distance, and suggest that this structure should be relatively high in energy in the protein matrix given the significant difference between QM and QM/MM iron-iron distances.

For the Aμ-1,2H_{peroxo} structure, based on the results from model compounds,[26, 91, 92] three kinds of conformers might be considered depending on the value of the dihedral angle defined by the irons and oxygen atoms (Figure 8). Our QM/MM calculations evaluated these three different conformers in the protein environment. The cis conformer (Figure 8) was discarded since it is higher in energy by 10–15 kcal/mol than its counterparts. The two gauche structures have similar energies, and their Fe-O-O-Fe units resemble the structure of a model compound studied by Kim and Lippard[26] in which the corresponding dihedral angles is 53°. In the discussion below, we only describe the lowest energy structure (top middle in Figure 8).

The correspondence between the structure of Aμ-1,2 H_{peroxo} and those of the μ-η^2,η^2 H_{peroxo} and μ-η^2,η^1 H_{peroxo} is quite good. Their respective RMSDs are 0.24 Å and 0.19 Å ignoring the peroxide moiety and Glu 243 in the case of μ-η^2,η^2 H_{peroxo}. This good agreement is also reflected by the Fe-Fe distance (Table 3), since the value in Aμ-1,2H_{peroxo} is essentially the same as found in μ-η^2,η^2 H_{peroxo}. Therefore, the Aμ-1,2 H_{peroxo} structure seems to be a reasonable candidate for the H_{peroxo} intermediate in the protein environment. But the geometries of the peroxide moieties in the three structures are very different. The Aμ-1,2 and μ-η^2,η^1 structures display short oxygen-oxygen distances (1.33 Å and 1.38 Å respectively), whereas in the μ-η^2,η^2 structure this distance is substantially greater (1.49 Å). Based on compounds present in the Cambridge Structural Database,[93] these distances clearly indicate that the Aμ-1,2 and μ-η^2,η^1 structures are more consistent with a superoxo species (1.33 Å), whereas the peroxo μ-η^2,η^2 structure actually resembles a peroxide (1.45 Å). This assignment is further supported by the electronic structure analysis below.

The singlet μ-η^2,η^2 butterfly structure affords two pseudo-octahedral environments at the iron atoms. Five virtual orbitals are centered on each iron atom and one empty σ* orbital is centered on the dioxygen moiety. This electronic structure is consistent with two anti-ferromagnetically coupled high-spin Fe(III) atoms, as found experimentally,[20, 21] in octahedral environments.

On the other hand, the electronic structure of Aμ-1,2 H_{peroxo} can best be described as intermediate between a superoxo and a peroxo species because the second electron transfer does not appear to have been completed. Analysis of the orbitals shows that a π* orbital of dioxygen is not totally filled and that Fe1 is still partly in its reduced state (see Supporting Information). Thus, Aμ-1,2 H_{peroxo} is more consistent with a superoxo structure with strong charge transfer from Fe1(II) to the dioxygen moiety. The electronic structures of the μ-η^2,η^1 H_{peroxo} and Sμ-1,2H_{peroxo} species are also better described as a superoxo species (see Supporting Information).

To characterize further the differences between the μ-η^2,η^2 butterfly and the cis-μ-1,2 H_{peroxo} structures, we have also analyzed the frequencies corresponding to the O-O and Fe-O stretching modes for both $^{16}O_2$ and $^{18}O_2$ to determine the isotopic shift (a B3LYP/6-31G* scaling factor of 0.9614[94] was used for all frequencies). In case of the cis-μ-1,2 H_{peroxo}, a ν (^{16}O-^{16}O) frequency of 1004 cm^{-1} was computed, compared to a value of 888 cm^{-1} for a model compound[26] (Table 4). A shift of 48 cm^{-1} was found in the case of the doubly isotopically substituted $^{18}O_2$, in good agreement with the shift of 46 cm^{-1} observed experimentally.[26] The ν(Fe-^{16}O) frequency was computed to be 441 cm^{-1} with an isotopic shift of 20 cm^{-1}, compared to 415 cm^{-1} [$\Delta^{18}O=11cm^{-1}$][26] for the experimental results. In case of the μ-η^2,η^2 H_{peroxo} structure, we obtained a ν(^{16}O-^{16}O) frequency of 815 cm^{-1} and a ν(Fe-^{16}O) value of 544 cm^{-1} with isotopic shifts of 44 cm^{-1} and 15 cm^{-1} respectively. There is currently no model complex with this structure.

The higher ν(^{16}O-^{16}O) frequency found for the cis-μ-1,2 H_{peroxo} compared to the μ-η^2,η^2 H_{peroxo} structure reveals its greater O-O bond order, and thus supports the superoxide character revealed by the electronic structure analysis. Compared to experiment, our calculations reveal enhanced superoxide character for this structure in the protein. In order to investigate whether a basis set effect was responsible for this behavior, the QM/MM models for the cis-μ-1,2 and the μ-η^2,η^2 H_{peroxo} models were optimized again by using the lacv3p** basis set on iron atoms and the cc-pVTZ(-f)++ on both oxygen atoms of the peroxide. The frequency calculations were then performed with the same modifications to the usual basis set. The results obtained show that, from a structural point of view, the basis set has an effect since the peroxo oxygen-oxygen distance increases from 1.33 Å to 1.37 Å in case of the cis-μ-1,2 H_{peroxo} and from 1.49 Å to 1.51 Å in the case of the μ-η^2,η^2 structure. These results indicate that the superoxo character of the cis-μ-1,2 H_{peroxo} is overestimated without the use of large basis sets (including diffuse functions) on the diiron core. Furthermore, the theoretical frequencies obtained with the large basis sets are in better agreement with experimental results on model compounds even without scaling (Table 4). For instance, the ν(^{16}O-^{16}O) frequency of the cis-μ-1,2 H_{peroxo} structure decreases to 975 cm^{-1} due to the decreased superoxo character, but it is still not enough to reach a good agreement with the model compound (888 cm^{-1}).

The frequency obtained for the cis-μ-1,2 H_{peroxo} structure indicates that it has a strong superoxo character, even when large basis sets are used. This frequency is intermediate between the ranges of experimental frequencies usually assigned to peroxo and to superoxo as defined by Suzuki *et al.*[95] based on different molecular oxygen complexes.

Intermediate Q—The last step of dioxygen activation involves reduction of H_{peroxo} by the transfer of two electrons from iron atoms leading to the cleavage of the O-O bond. The resulting di(μ-oxo)diiron(IV) structure (H_Q) can formally be described as two O^{2-} ions coordinated to two Fe(IV) cations.

The main difference observed between structures obtained at the QM/MM level and at the QM level (RMSD of 0.73 Å between them) are rotations of Glu 209 and Glu 114 leading to slight differences in the structure of the $Fe_2(\mu\text{-}O)_2$ quadrilateral. Interestingly, in the QM/MM model, the Fe-O distances appear to be somewhat asymmetric with the oxygen atoms both being closer to Fe1 than to Fe2, with average distances of 1.75 Å and 1.90 Å respectively (Figure 9). Asymmetry has also been reported from an analysis of the results of EXAFS experiments on H_Q.[31] Our calculations reveal that the two iron centers are not equivalent, indicating a slightly diminished (between Fe^{IV} and Fe^{III}) oxidation state for Fe2 as compared to Fe1 (Fe^{IV}). This results from the fact that Fe2 appears to be slightly more electrophilic than Fe1 and thus attracts more the electrons from the oxygen atoms. This is consistent with our previous study[89] showing that Fe2 is actually the first iron atom reduced during the reaction between H_Q and methane. The iron-iron distance is larger in the QM/MM models (2.84 Å) than in the QM one (2.70 Å) and significantly larger than found by the analysis of the EXAFS data (2.46 Å).[31] Our QM models have also shown that the singlet state has nearly symmetric Fe-O distances (1.76 Å and 1.82 Å), whereas in the nonet state these bonds were very asymmetric (1.69 Å and 2.13 Å). The analysis indicates this result is derived from a higher oxidation level of Fe1 compared to Fe2 (formally a Fe^{V}-Fe^{III} core) (see Supporting Information).

The electronic structure obtained for the singlet state of H_Q is in good agreement with that expected for a di(μ-oxo)diiron(IV) species and has been presented in a previous paper.[89] Nonetheless, compared to the $\mu\text{-}\eta^2,\eta^2$ butterfly H_{peroxo}, strong delocalization of oxo electrons onto the iron atoms can be noticed, supporting an increased covalency between iron and oxygen atoms as has recently been proposed based on oxoiron(IV) model compounds.[96, 97]

Energetic analysis

In this section we analyze the energies of our computed reaction cycle components comparing relative energies for QM/MM with the purely QM models discussed in ref. [[19]]. We consider all states discussed above with the exception of that in which the water is displaced from the cavity prior to binding of dioxygen. This state is not experimentally accessible, and there are considerable complexities in dealing with the free energies of binding of small molecules to the protein. Furthermore, examination of the reduced MMO crystal structure reveals a different number of waters in the cavities of the two α-subunit protomers, and the presence or absence of a second water molecule would have a significant effect on the calculated free energies of the state in question.

Along the same lines, we note that energy differences between the reduced enzyme and oxygenated intermediates also involve an estimation of the binding affinity of dioxygen to the protein. As indicated above, these quantities are subject to some uncertainty, so our expectation is that the calculation of the relative energy of the reduced enzyme compared to the other species will have increased error bars due to these issues.

The large basis set QM/MM//UDFT single point energies, supplemented by frequency calculations on models as discussed above, provide the starting point for our energetic analysis. We have additionally investigated the effects of two types of correction terms. Firstly, we constructed a Heisenberg spin model in order to improve the relative energetics of AF spin states as modeled via broken symmetry and unrestricted wave functions; details of the methodology are given in Supporting Information. Secondly, we introduce a new set of corrections based on the localized orbital correction (LOC) approach discussed earlier. LOC assigns correction parameters for atomic hybridization states and for each electron pair in a bonding orbital, depending upon the type of bond and its local environment. Our assessment of the relative energetics of structures in the MMO catalytic cycle utilizes the following key parameters of the methodology, derived from fitting to the G3 data set as discussed in detail in ref. [[78]]:

1. An O atom is assigned a correction factor of 1.8 kcal/mol when sp^3 hybridized, and 1.0 kcal/mol when sp^2 hybridized.
2. An ordinary O-O single bond is assigned a correction factor of −2.0 kcal/mol and a double bond, −1.0 kcal/mol.
3. An ionic bond (NaCl is the prototypical example) is assigned a correction factor of −4.5 kcal/mol. This parameter works remarkably well for a wide range of “ionic” pairs, not only NaCl but formal charge separations assigned on the basis of classical valence bond theory as, for example, in CO or ozone. The success in describing ozone is particularly relevant to the present task; the corrected B3LYP-LOC atomization energy error is only −1.87 kcal/mol whereas the B3LYP error is 8.6 kcal/mol.

The physical rational for these corrections is based on the localized nature of the residual errors in DFT methods, which arise from erroneous treatment of nondynamical correlations of both unpaired and paired electrons. For electron pairs, B3LYP underestimates nondynamical correlation when the “size” of the localized orbital containing the pair is “small” compared to the bond length. The discrepancy is particularly large for ionic bonds with long distances, as is the case here for a subset of the Fe-O interactions. The number of ionic (non-covalent) electron pairs on the core oxygen atoms increases as one goes from $H_{superoxo}$ (one) to H_{peroxo} (two) to H_Q (four) and hence, according to the theory, the total energy of these species is increasingly overestimated. We argue below that the correction terms restore the proper relative energetics of our intermediates.

Results obtained from our QM/MM B3LYP calculations using the high level basis set with diffuse functions on dioxygen atoms are presented in Table 5 for all species found to be relevant at a lower computational level. The Heisenberg exchange coupling constants (Table 6) were calculated for H_{red}, H_{peroxo} and H_Q. Moreover, in the case of $H_{superoxo}$, the formula for spin-projection cannot be applied because the metals are not equivalent, but the error induced by neglecting spin projection should be small since the differences between high-spin and broken symmetry energies are rather insignificant (less than 1 kcal/mol).

The relative energies of intermediates found in our QM/MM calculations, presented in Figure 10, are qualitatively comparable with those along the best path previously identified.[19] Some quantitative differences emerged, however, between the present QM/MM study and our previous purely QM models.

First, we re-evaluated μ-1,2 models for the controversial structure of the H_{peroxo} intermediate. Our results show that the Aμ-1,2 H_{peroxo} structure appears to be slightly higher in energy compared to the μ-η^2,η^2 species (Table 5). Nonetheless, given the relatively small energy difference, this structure might be a putative intermediate between $H_{superoxo}$ and the μ-η^2,η^2 form of H_{peroxo}. On the other hand, the Sμ-1,2 H_{peroxo} species which lacks a bridging atom between the iron atoms, was computed to be much higher in energy than the μ-η^2,η^2 structure at the QM/MM//RDFT level. This species was therefore discarded as a possible intermediate in the reaction mechanism and further calculations were not performed on it.

The second main difference between the QM and QM/MM calculations is related to the relative energy between μ-η^2,η^2 H_{peroxo} and H_Q. Actually, in our QM/MM calculations (Table 5), H_Q is higher in energy than H_{peroxo} by 0.7 kcal/mol. This result is surprising because experimentally H_Q can be kinetically trapped[3, 8] and the reaction should thus be exothermic, presumably by a significant margin compared to kT, or one would see residual population of H_{peroxo} experimentally. Previous authors using different computational models have encountered the same problem.[98, 99] Moreover, our new results are in contradiction to our previous findings reported in ref. [[19]], in which H_Q was 11.7 kcal/mol[19] lower in energy than H_{peroxo}. The reason for this discrepancy has been identified as a structural difference between our QM/MM models of H_Q and the large QM model previously employed.[19] In our QM models, Asp 242-Glu 243 peptide displays a different conformation than that in the crystallographic structures[80, 81, 87] or other QM or QM/MM models (See Supporting Information Figure S-17). As pointed out by Siegbahn,[100] this previous conformation allows the formation of a new hydrogen bond between the dangling oxygen atom of Glu 243 and a backbone N-H unit. To check whether this new hydrogen bond was responsible for the significant stabilization of H_Q over H_{peroxo} in our large QM models in ref. [[19]], we constructed a big QM model of H_{peroxo} with the same backbone conformation. Our results reveal that this hydrogen bond also strongly lowers the energy of H_{peroxo}. However, the present QM/MM calculations indicate that such a hydrogen bond does not form inside the protein for either H_Q or H_{peroxo} due to the constraints and hydrogen bond network generated by the protein fold which are not present in the purely QM models. Thus the overstabilization of H_Q due to this hydrogen bond is no longer possible in the QM/MM models, and H_Q becomes slightly less stable than H_{peroxo} when calculated with the B3LYP density functional, as indicated above.

Because the above QM/MM results for the relative energies of H_{peroxo} and H_Q were in disagreement with experiment, we investigated whether this discrepancy could be explained by the intrinsic errors of B3LYP. We applied the B3LYP-LOC scheme outlined above, with simple approximations as discussed in Supporting Information, to the results obtained for all the structures previously found to be relevant for the dioxygen activation reaction. These findings are presented in Table 7. As can be seen, the corrections of the B3LYP-LOC scheme favor the dioxygen activation by MMO as a whole, because the series of intermediates contains an increasing component of charge transfer from the iron to the dioxygen atoms in the core (Figure 10). The correction is particularly important for the relative energies of H_{peroxo} and H_Q. We can see that, with B3LYP-LOC, H_Q is much more stabilized than H_{peroxo}. Based on this preliminary analysis, B3LYP errors may be the reason for the lower energy of H_{peroxo} compared to H_Q reported above. We hypothesize that these errors mainly arise due to underestimation of the contribution of ionic character bonds in using standard B3LYP results and the fact that these bonds are strongly involved in the dioxygen activation reaction.

Discussion

Nature of the H_{peroxo} intermediate

Several structures for H_{peroxo} have been investigated in this study. The results obtained allow us to discard the Sμ-1,2(1) H_{peroxo} based on its high energy compared to the other structures. It lacks a bridging ligand between the iron atoms that stabilizes the other structures. The QM/MM//RDFT results show that the μ-η^2,η^2 H_{peroxo} and the Aμ-1,2 H_{peroxo} species are very similar in energy, whereas the μ-η^2,η^1 H_{peroxo} is slightly higher. Finally, our QM/MM//UDFT results indicate that the μ-η^2,η^2 H_{peroxo} is actually lower in energy than the Aμ-1,2 H_{peroxo} by 2.8 kcal/mol in the protein environment.

In the case of a ribonucleotide reductase variant,[90] the peroxo intermediate has a cis-μ-1,2 peroxo diiron(III) core structure. Although our pure QM calculations are compatible with such a hypothesis for H_{peroxo}, QM/MM models reveal that this structure is destabilized in the protein. Analysis shows that the main differences involve the two histidines which rotate in the QM model, and Glu 243, which forms a much better bridge in the QM structure. An important difference between the QM and QM/MM models is the 0.10 Å shorter iron-iron distance in the latter. This distance is consistent with the effect of the protein observed for all the species involved in the O_2 activation, from which, the energy discrepancy between the QM and QM/MM models can be rationalized. The energy of the Aμ-1,2 H_{peroxo} structure should be more sensitive to this distance because the overlap between the peroxo and iron orbitals will depend strongly on it. This point is supported by the fact that the Aμ-1,2 H_{peroxo} with a cis conformation ($\phi \sim 0$ in Figure 8) is strongly destabilized by including the protein in our models. Therefore, the fact that the μ-η^2,η^2 core structure is preferred over the Aμ-1,2 H_{peroxo} structure in MMOH appears to be a consequence of the fact that strain induced by the protein environment decreases the iron-iron distance.

As noted by Solomon *et al.*,[90] it is difficult to understand the similarity between the optical absorption spectra of the peroxo species in MMOH and RNR-R2 given that they have different binding modes. One possibility is that two peroxide species may be formed along the O_2 activation pathway. The energetics obtained in the current study and the sequence of structural and electronic changes that occur along the cycle are not inconsistent with such a hypothesis. Indeed, all our analyses of the Aμ-1,2 H_{peroxo} and the μ-η^2,η^2 structures support the fact that the latter has a true peroxo nature whereas the former is intermediate between a superoxo and a peroxo species. The fact that Aμ-1,2 H_{peroxo} prevents a complete electron transfer to give a true peroxo species makes it a poor candidate for generating $H_{Q,}$ which requires such a new electron transfer. In this context the μ-η^2,η^2 structure appears to be a much better candidate for the intermediate preceding the formation of H_Q. Notably, a Q-type intermediate does not appear to form in ribonucleotide reductase. Possibly MMOB is involved in stabilizing the H_{peroxo} form that converts to H_Q. The possibility that two peroxo intermediates occur has been previously proposed by Lippard *et al.*[23] to explain the discrepancy between the rates of formation of H_{peroxo} as determined by stopped-flow optical spectroscopy and by Mössbauer or optical spectroscopy.

To summarize, our QM/MM calculations are in better agreement with a μ-η^2,η^2 structure for H_{peroxo} prior the formation of H_Q, and do not exclude the possible existence of another intermediate between $H_{superoxo}$ and H_{peroxo} having the structure of Aμ-1,2 H_{peroxo}.

QM/MM structure of H_Q

The structure obtained for H_Q in the current study features asymmetric coordination of the oxygen atoms that bridge the iron atoms, as was observed experimentally.[31] This result is particularly interesting because our previous calculations at the QM level yielded a symmetric structure for the singlet state. The nonet state, very close in energy, was strongly asymmetric. This asymmetric structure was shown to be better described in terms of an Fe(III)-Fe(V) diiron core, whereas the symmetric case was better represented as an Fe(IV)-Fe(IV) diiron core. The protein environment, and most likely its electrostatic field, is probably responsible of some kind of mixing between these two oxidation state extrema. The calculations also demonstrate that the electronic structure of H_Q is particularly sensitive to the chemical environment since the geometry of the diiron core changes depending on the coupling chosen for the diiron core, and whether or not the protein is included in the model.

Role of the protein in dioxygen activation

The most interesting finding of the present QM/MM calculations is that the protein seems to play an active role in the catalysis, principally by differentially compressing the Fe-Fe distance for the various species in the catalytic cycle. This effect is consistently observed along the path from H_{red} to H_{peroxo} (Table 3). It has also been observed for H_{red} using ONIOM methods[50] but, whereas with our QM/MM methodology the agreement with the experimental Fe-Fe distance is very good (~ 0.02 Å), the results with ONIOM method were significantly less accurate (0.15–0.25 Å), probably due to quantitative errors in the QM/MM interface model employed in ref. [[50]].

From an energetic point of view, the effect of the protein is to decrease (make more negative relative to H_{red}) the energy of species between H_{red} and H_{peroxo} (Table 5 and discussion on the QM/MM//RDFT calculations in Supporting Information). It is therefore tempting to correlate stabilization with compression of the iron-iron distance. In this sense, the most reasonable explanation for the effect of the protein would be that it preferentially destabilizes H_{red} because the largest compression of the iron-iron distance is observed for this species. This strain energy is then released along the reaction pathway until arriving at H_{peroxo}. This hypothesis, previously suggested by several authors,[41, 49] is strongly supported by our current results.

It is interesting that the protein appears to increase, rather than decrease, the Fe-Fe distance for our model of H_Q (by 0.14 Å). From a physical point of view, this result is not necessarily inconsistent with the behavior of the remaining species; the gas phase Fe-Fe separation for H_Q is substantially shorter than for any other structure, so if the protein forces are generated by an effective harmonic model with an implicit equilibrium distance intermediate between this value (2.70 Å) and the typical gas phase separation in the remaining species (~3.5 Å), the observed results can easily be rationalized. It is beyond the scope of the present paper to analyze the protein forces in sufficient detail to establish whether this picture is correct, but such an investigation is possible in principle, and will be considered in future publications.

There is finally, as noted above, an apparently large discrepancy between the calculated Fe-Fe distance for H_Q (2.84 Å) and the value extracted from analysis of EXAFS data in ref. [[31]] (2.46 Å). The excellent agreement that we now obtain for the structure of H_{red} with the crystallographic data of ref. [[86]] provides some confidence that the B3LYP/QM/MM methodology employed herein is capable of generating accurate structural predictions, given a reasonable initial starting geometry and electronic wavefunction. At the moment, we have to regard this discrepancy as an unresolved problem, with a number of possible solutions: (1) the structure of Q might be qualitatively different from what we assume here (although we are not aware of other plausible candidate structures with competitive energies that have been proposed); (2) the binding of MMOB might significantly alter the active site geometry, resulting in the reduction of the Fe-Fe distance; (3) There may be some difficulties in the interpretation of the EXAFS data. All of these avenues will need to be pursued in order to achieve convergence of theory and experiment.

Conclusion

The present theoretical QM/MM models reveal how the protein matrix can influence the diiron active site of MMOH by compressing the iron-iron distance. The energetic consequences are that the intermediates closer to the reduced form in the proposed reaction pathway (Figure 11) are more destabilized by the protein than those closer to H_Q.

Different structures were investigated for H_{peroxo}. The results obtained with QM/MM models reveal that the cis-μ-1,2 H_{peroxo} is 2.8 kcal/mol higher in energy than the μ-η^2,η^2 H_{peroxo} structure. Electronic structure and frequency calculations revealed that the cis-μ-1,2 H_{peroxo}

species is intermediate between a superoxo and a peroxo species. These results suggest that a cis-μ-1,2 H_{peroxo} intermediate could precede the formation of the μ-η^2,η^2 butterfly structure.

Very close energies were found for the μ-η^2,η^2 H_{peroxo} and H_Q intermediates. By applying the B3LYP-LOC scheme recently developed in our laboratory, we suggested that this result is a consequence of systematic errors in the B3LYP functional. Although preliminary results obtained by applying a highly approximate version of our B3LYP-LOC methodology to the problem are encouraging, further investigation will required to ascertain the quantitative value of these corrections.

Supplementary Material

Refer to Web version on PubMed Central for supplementary material.

Acknowledgements

This work was supported in part by grants from the NIH to RAF (GM40526) and SJL (GM32134). We thank Per Siegbahn for useful discussions concerning the relative energies of the H_{peroxo} and H_Q intermediates and DR thanks Benjamin Gherman and Laurance Beauvais for their advice and for helpful discussions. This research was performed in part using the Molecular Science Computing Facility (MSCF) in the William R. Wiley Environmental Molecular Sciences Laboratory, a national scientific user facility sponsored by the U.S. Department of Energy's Office of Biological and Environmental Research and located at the Pacific Northwest National Laboratory, operated for the Department of Energy by Battelle. This work was partially supported by the National Center for Supercomputing Applications under CHE040019 and utilized the IBM pSeries 690.

References

1. Feig AL, Lippard SJ. Chem Rev 1994;94:759.
2. Liu KE, Lippard SJ. Adv Inorg Chem 1995;42:263.
3. Wallar BJ, Lipscomb JD. Chem Rev 1996;96:2625. [PubMed: 11848839]
4. Valentine AM, Lippard SJ. J Chem Soc Dalton Trans 1997:3925.
5. Deeth RJ, Dalton H. J Biol Inorg Chem 1998;3:302.
6. Whittington, DA.; Lippard, SJ. Handbook of metalloproteins. 2. John Wiley & Sons; Chichester: 2001. Methane monooxygenase hydroxylase; p. 712
7. Kopp DA, Lippard SJ. Curr Opin Chem Biol 2002;6:568. [PubMed: 12413539]
8. Merkx M, Kopp DA, Sazinsky MH, Blazyk JL, Muller J, Lippard SJ. Angew Chem, Int Ed 2001;40:2782.
9. Merkx M, Lippard SJ. J Biol Chem 2002;277:5858. [PubMed: 11709550]
10. Crabtree RH. J Chem Soc, Dalton Trans 2001:2951.
11. Periana RA, Bhalla G, Tenn WJ, Young KJH, Liu XY, Mironov O, Jones CJ, Ziatdinov VR. J Mol Catal A 2004;220:7.
12. van Beilen JB, Funhoff EG. Curr Opin Biotechnol 2005;16:308. [PubMed: 15961032]
13. Friesner RA, Baik MH, Gherman BF, Guallar V, Wirstam M, Murphy RB, Lippard SJ. Coord Chem Rev 2003;238:267.
14. Baik MH, Newcomb M, Friesner RA, Lippard SJ. Chem Rev 2003;103:2385. [PubMed: 12797835]
15. Noodleman L, Lovell T, Han WG, Li J, Himo F. Chem Rev 2004;104:459. [PubMed: 14871132]
16. Siegbahn PEM. J Biol Inorg Chem 2001;6:27. [PubMed: 11191221]
17. Torrent M, Musaev DG, Basch H, Morokuma K. J Comput Chem 2002;23:59. [PubMed: 11913390]
18. Yoshizawa K. J Inorg Biochem 2000;78:23. [PubMed: 10714702]
19. Gherman BF, Baik MH, Lippard SJ, Friesner RA. J Am Chem Soc 2004;126:2978. [PubMed: 14995216]
20. Liu KE, Wang DL, Huynh BH, Edmondson DE, Salifoglou A, Lippard SJ. J Am Chem Soc 1994;116:7465.

21. Liu KE, Valentine AM, Wang DL, Huynh BH, Edmondson DE, Salifoglou A, Lippard SJ. J Am Chem Soc 1995;117:10174.
22. Liu KE, Valentine AM, Qiu D, Edmondson DE, Appelman EH, Spiro TG, Lippard SJ. J Am Chem Soc 1995;117:4997.
23. Valentine AM, Stahl SS, Lippard SJ. J Am Chem Soc 1999;121:3876.
24. Lee SY, Lipscomb JD. Biochemistry 1999;38:4423. [PubMed: 10194363]
25. Brazeau BJ, Lipscomb JD. Biochemistry 2000;39:13503. [PubMed: 11063587]
26. Kim K, Lippard SJ. J Am Chem Soc 1996;118:4914.
27. Micklitz W, Bott SG, Bentsen JG, Lippard SJ. J Am Chem Soc 1989;111:372.
28. Menage S, Brennan BA, Juarezgarcia C, Münck E, Que L Jr. J Am Chem Soc 1990;112:6423.
29. Brennan BA, Chen QH, Juarezgarcia C, True AE, O'connor CJ, Que L Jr. Inorg Chem 1991;30:1937.
30. Lee SK, Fox BG, Froland WA, Lipscomb JD, Münck E. J Am Chem Soc 1993;115:6450.
31. Shu LJ, Nesheim JC, Kauffmann K, Münck E, Lipscomb JD, Que L Jr. Science 1997;275:515. [PubMed: 8999792]
32. Lee SK, Nesheim JC, Lipscomb JD. J Biol Chem 1993;268:21569. [PubMed: 8408008]
33. Priestley ND, Floss HG, Froland WA, Lipscomb JD, Williams PG, Morimoto H. J Am Chem Soc 1992;114:7561.
34. Shteinman AA. FEBS Lett 1995;362:5. [PubMed: 7698352]
35. Lipscomb JD, Que L Jr. J Biol Inorg Chem 1998;3:331.
36. Nordlander E, Andersson KK. J Biol Inorg Chem 1998;3:300.
37. Shteinman AA. J Biol Inorg Chem 1998;3:325.
38. Whittington DA, Valentine AM, Lippard SJ. J Biol Inorg Chem 1998;3:307.
39. Gherman BF, Goldberg SD, Cornish VW, Friesner RA. J Am Chem Soc 2004;126:7652. [PubMed: 15198613]
40. Valentine AM, Wilkinson B, Liu KE, Komar-Panicucci S, Priestley ND, Williams PG, Morimoto H, Floss HG, Lippard SJ. J Am Chem Soc 1997;119:1818.
41. Dunietz BD, Beachy MD, Cao YX, Whittington DA, Lippard SJ, Friesner RA. J Am Chem Soc 2000;122:2828.
42. Guallar V, Gherman BF, Miller WH, Lippard SJ, Friesner RA. J Am Chem Soc 2002;124:3377. [PubMed: 11916423]
43. Lovell T, Han WG, Liu TQ, Noodleman L. J Am Chem Soc 2002;124:5890. [PubMed: 12010064]
44. Lovell T, Li J, Noodleman L. Inorg Chem 2001;40:5251. [PubMed: 11559090]
45. Lovell T, Li J, Noodleman L. Inorg Chem 2001;40:5267. [PubMed: 11559091]
46. Torrent M, Musaev DG, Morokuma K. J Phys Chem B 2001;105:322.
47. Yoshizawa K, Hoffmann R. Inorg Chem 1996;35:2409. [PubMed: 11666447]
48. Yumura T, Yoshizawa K. Bull Chem Soc Jpn 2004;77:1305.
49. Torrent M, Vreven T, Musaev DG, Morokuma K, Farkas O, Schlegel HB. J Am Chem Soc 2002;124:192. [PubMed: 11782169]
50. Hoffmann M, Khavrutskii IV, Musaev DG, Morokuma K. Int J Quantum Chem 2004;99:972.
51. *QSite* 2.7 Schrödinger Inc., Portland OR, 2003.
52. Murphy RB, Philipp DM, Friesner RA. Chem Phys Lett 2000;321:113.
53. Murphy RB, Philipp DM, Friesner RA. J Comput Chem 2000;21:1442.
54. Philipp DM, Friesner RA. J Comput Chem 1999;20:1468.
55. Jaguar 5.5 Schrödinger, Inc.; Portland OR: 2003.
56. IMPACT 2.7 Schrödinger Inc.; Portland OR: 2003.
57. Banks JL, et al. J Comput Chem 2005;26:1752. [PubMed: 16211539]
58. Jorgensen WL, Maxwell DS, TiradoRives J. J Am Chem Soc 1996;118:11225.
59. Kaminski GA, Friesner RA, Tirado-Rives J, Jorgensen WL. J Phys Chem B 2001;105:6474.
60. Guallar V, Friesner RA. J Am Chem Soc 2004;126:8501. [PubMed: 15238007]

61. Guallar V, Baik MH, Lippard SJ, Friesner RA. Proc Natl Acad Sci U S A 2003;100:6998. [PubMed: 12771375]
62. Wirstam M, Lippard SJ, Friesner RA. J Am Chem Soc 2003;125:3980. [PubMed: 12656634]
63. Guallar V, Jacobson M, McDermott A, Friesner RA. J Mol Biol 2004;337:227. [PubMed: 15001364]
64. QSite 4.0 alpha Schrödinger Inc.; Portland OR: 2005.
65. Gherman BF, Lippard SJ, Friesner RA. J Am Chem Soc 2005;127:1025. [PubMed: 15656641]
66. Parr, RG.; Yang, W. Density Functional Theory of Atoms and Molecules. Oxford University Press; New York: 1989.
67. Becke AD. J Chem Phys 1993;98:1372.
68. Johnson BG, Gill PMW, Pople JA. J Chem Phys 1993;98:5612.
69. Lee CT, Yang WT, Parr RG. Phys Rev B 1988;37:785.
70. Friesner RA, Dunietz BD. Acc Chem Res 2001;34:351. [PubMed: 11352713]
71. Friesner RA, Murphy RB, Beachy MD, Ringnalda MN, Pollard WT, Dunietz BD, Cao YX. J Phys Chem A 1999;103:1913.
72. Vacek G, Perry JK, Langlois JM. Chem Phys Lett 1999;310:189.
73. Mainz DT, Klicic JJ, Friesner RA, Langlois JM, Perry JK. J Comput Chem 1997;18:1863.
74. Hay PJ, Wadt WR. J Chem Phys 1985;82:270.
75. Hay PJ, Wadt WR. J Chem Phys 1985;82:299.
76. Wadt WR, Hay PJ. J Chem Phys 1985;82:284.
77. Dunning TH. J Chem Phys 1989;90:1007.
78. Friesner RA, Knoll E, Cao Y. J Chem Phys 2006;125:124107. [PubMed: 17014166]
79. Curtiss LA, Raghavachari K, Redfern PC, Rassolov V, Pople JA. J Chem Phys 1998;109:7764.
80. Rosenzweig AC, Frederick CA, Lippard SJ, Nordlund P. Nature 1993;366:537. [PubMed: 8255292]
81. Rosenzweig AC, Nordlund P, Takahara PM, Frederick CA, Lippard SJ. Chem Biol 1995;2:409.
82. Humphrey W, Dalke A, Schulten K. J Mol Graphics 1996;14:33.
83. Maestro 6.01 Schrödinger, Inc; Portland OR: 2003.
84. Fox BG, Surerus KK, Münck E, Lipscomb JD. J Biol Chem 1988;263:10553. [PubMed: 2839495]
85. Hendrich MP, Münck E, Fox BG, Lipscomb JD. J Am Chem Soc 1990;112:5861.
86. Fox BG, Hendrich MP, Surerus KK, Andersson KK, Froland WA, Lipscomb JD, Münck E. J Am Chem Soc 1993;115:3688.
87. Whittington DA, Lippard SJ. J Am Chem Soc 2001;123:827. [PubMed: 11456616]
88. Cramer CJ, Tolman WB, Theopold KH, Rheingold AL. Proc Natl Acad Sci U S A 2003;100:3635. [PubMed: 12634422]
89. Baik MH, Gherman BF, Friesner RA, Lippard SJ. J Am Chem Soc 2002;124:14608. [PubMed: 12465971]
90. Skulan AJ, Brunold TC, Baldwin J, Saleh L, Bollinger JM, Solomon EI. J Am Chem Soc 2004;126:8842. [PubMed: 15250738]
91. Dong YH, Yan SP, Young VG, Que L Jr. Angew Chem, Int Ed 1996;35:618.
92. Ookubo T, Sugimoto H, Nagayama T, Masuda H, Sato T, Tanaka K, Maeda Y, Okawa H, Hayashi Y, Uehara A, Suzuki M. J Am Chem Soc 1996;118:701.
93. Allen FH, Taylor R. Chem Soc Rev 2004;33:463. [PubMed: 15480471]
94. Scott AP, Radom L. J Phys Chem 1996;100:16502.
95. Suzuki M, Ishiguro T, Kozuka M, Nakamoto K. Inorg Chem 1981;20:1993.
96. Rohde JU, Torelli S, Shan XP, Lim MH, Klinker EJ, Kaizer J, Chen K, Nam WW, Que L Jr. J Am Chem Soc 2004;126:16750. [PubMed: 15612713]
97. Jensen MP, Costas M, Ho RYN, Kaizer J, Payeras AMI, Münck E, Que L Jr, Rohde JU, Stubna A. J Am Chem Soc 2005;127:10512. [PubMed: 16045338]
98. Siegbahn PEM. Inorg Chem 1999;38:2880. [PubMed: 11671034]
99. Torrent M, Mogi K, Basch H, Musaev DG, Morokuma K. J Phys Chem B 2001;105:8616.
100. Siegbahn PEM, Borowski T. Acc Chem Res 2006;39:729. [PubMed: 17042473]

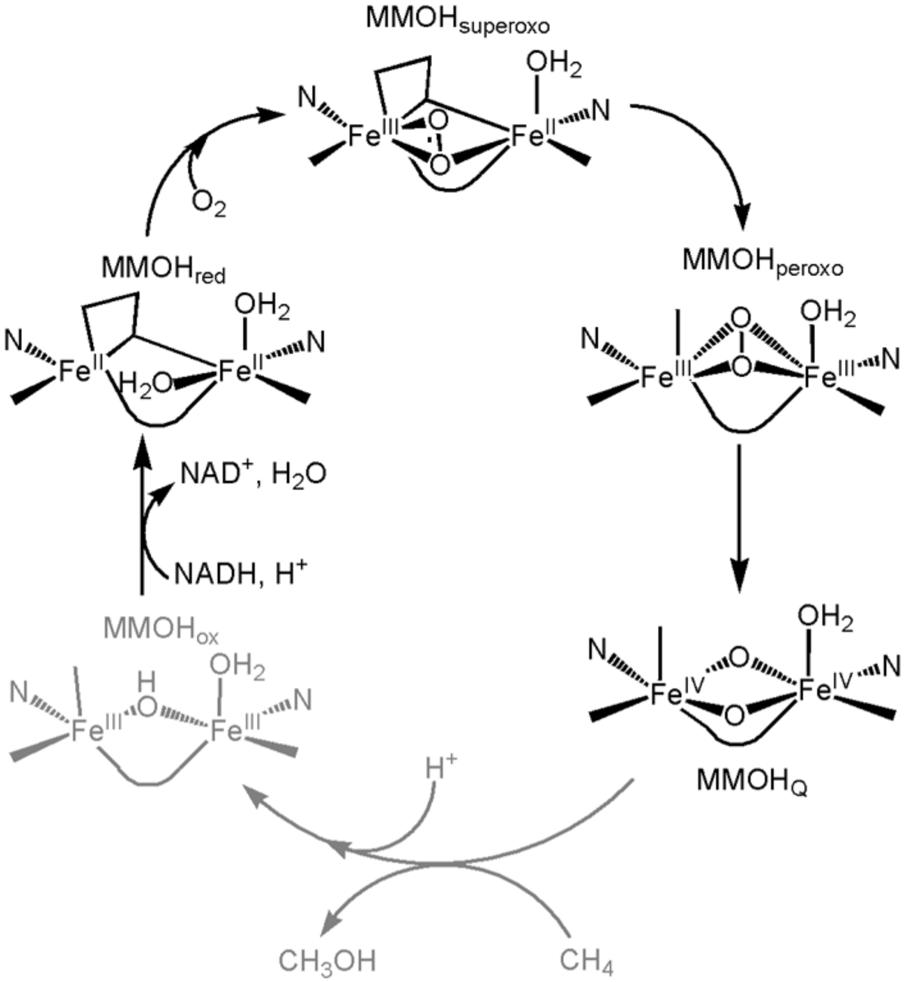

Figure 1.

The catalytic cycle of MMOH. The part of the cycle corresponding to activation of dioxygen is shown in black while the oxidation of the substrate (hydroxylation of methane into methanol *in vivo*) is in light gray.

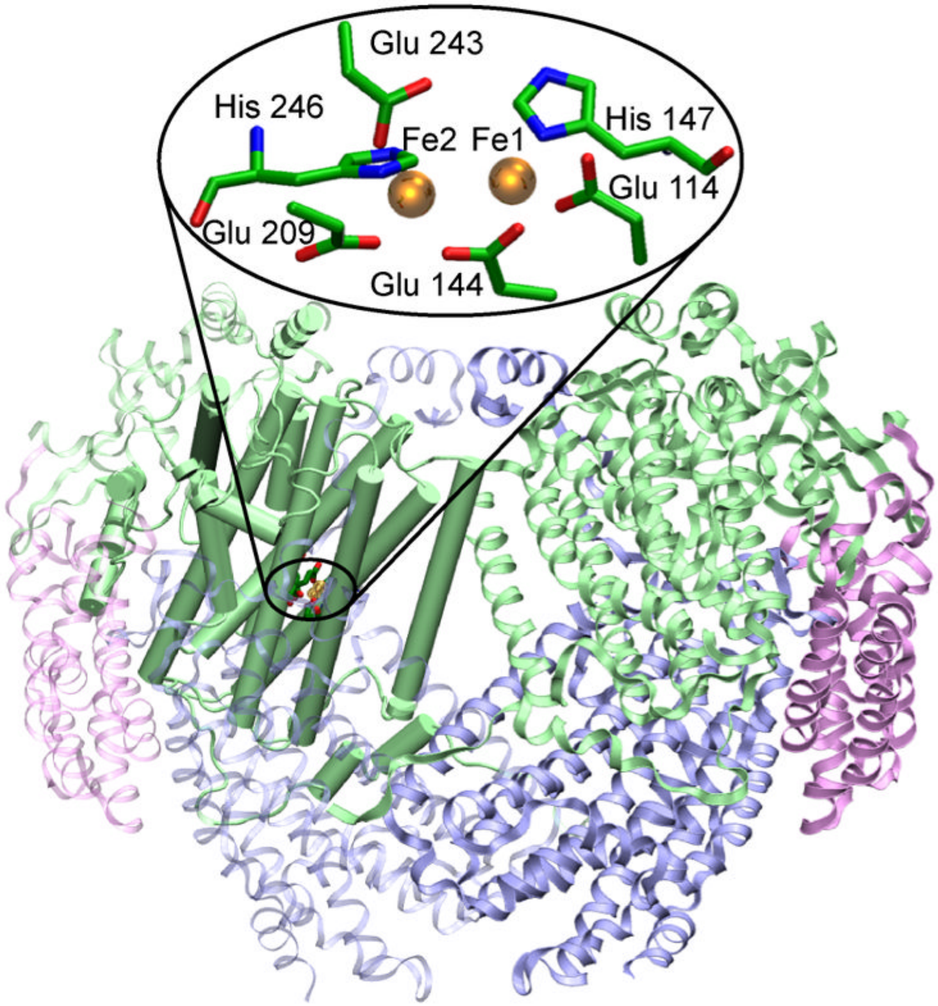

Figure 2.

Structure of the oxidized $\mathrm{MMOH_{ox}}$ protein (PDB code 1MTY) represented in ribbon. The α subunits are depicted in green, the β subunits in purple and the γ subunits in pink. The QM/MM model used is shown in cartoon representation and is made of a sphere of 35 Å of the α subunit of protomer α (chain D in PDB code 1MTY). The QM part is represented in licorice in the panel (Graphic prepared with VMD[82]). Solvent-derived ligands are omitted.

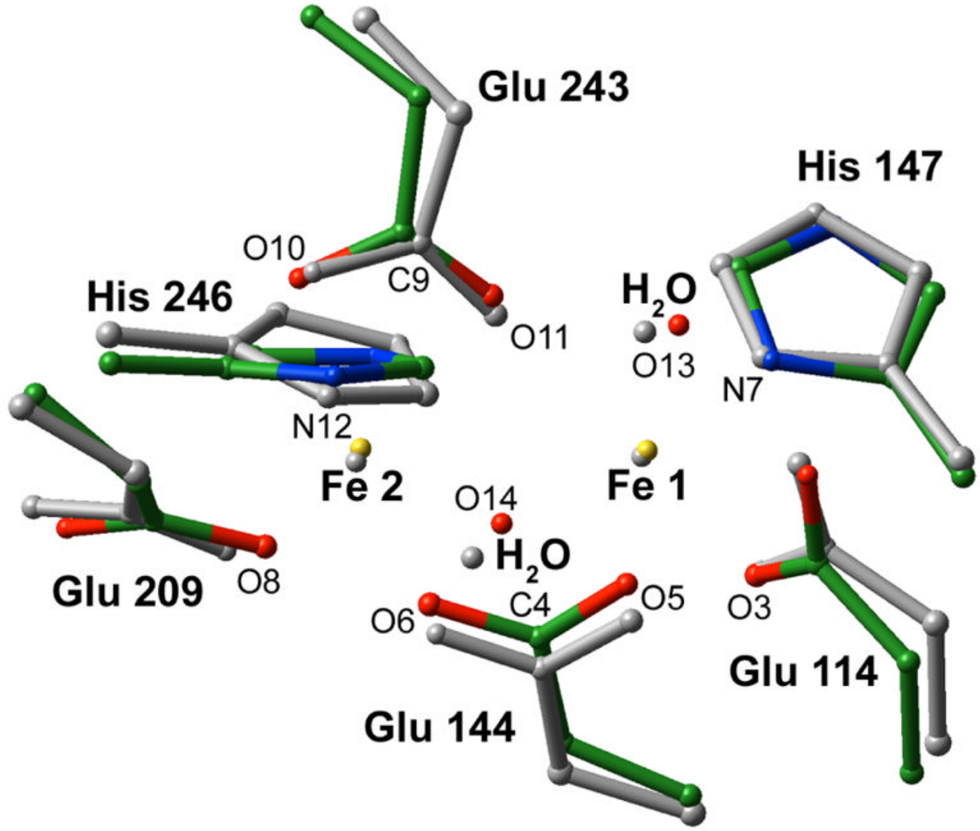

Figure 3.
Optimized QM/MM structure of Hred (color) superimposed onto the corresponding crystal structure (gray). The first shell atom names are also displayed.

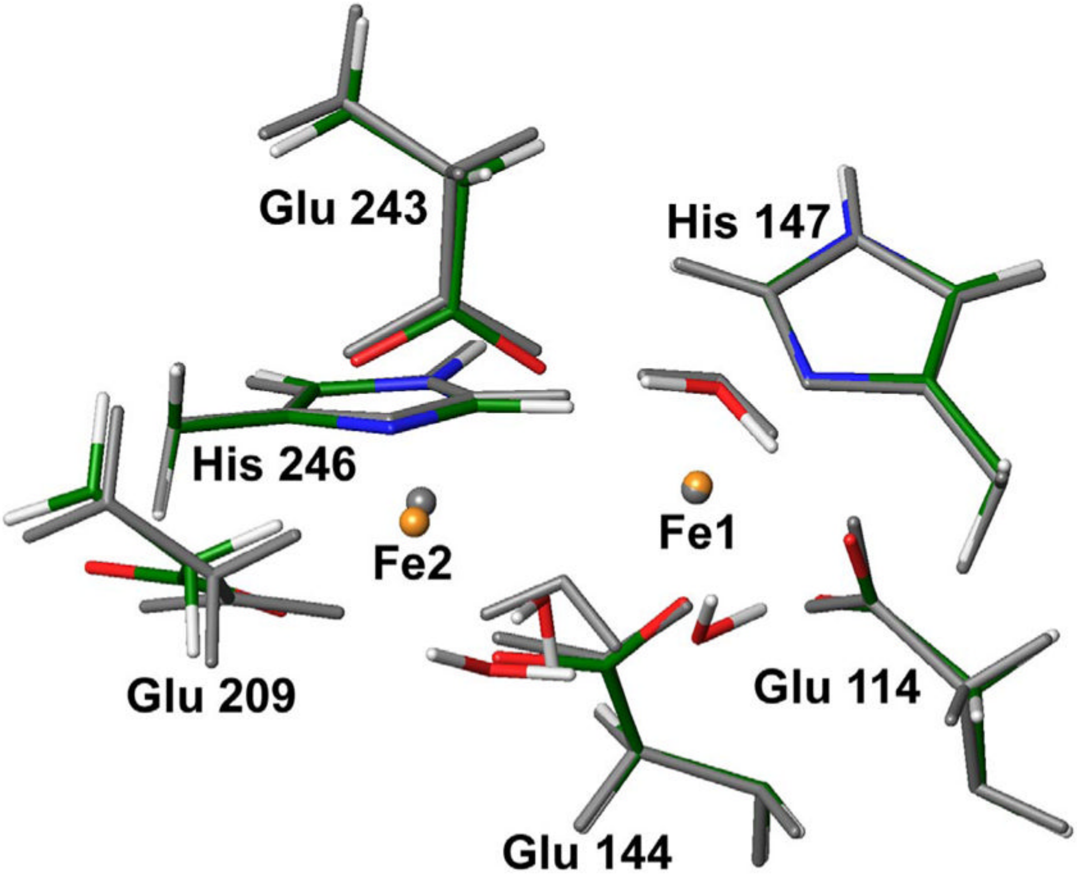

Figure 4.

QM/MM structure of Hred including two additional water molecules (color) superimposed onto the standard QM/MM model (gray). The two water molecules have an important effect on the position of Glu 209 and Fe2.

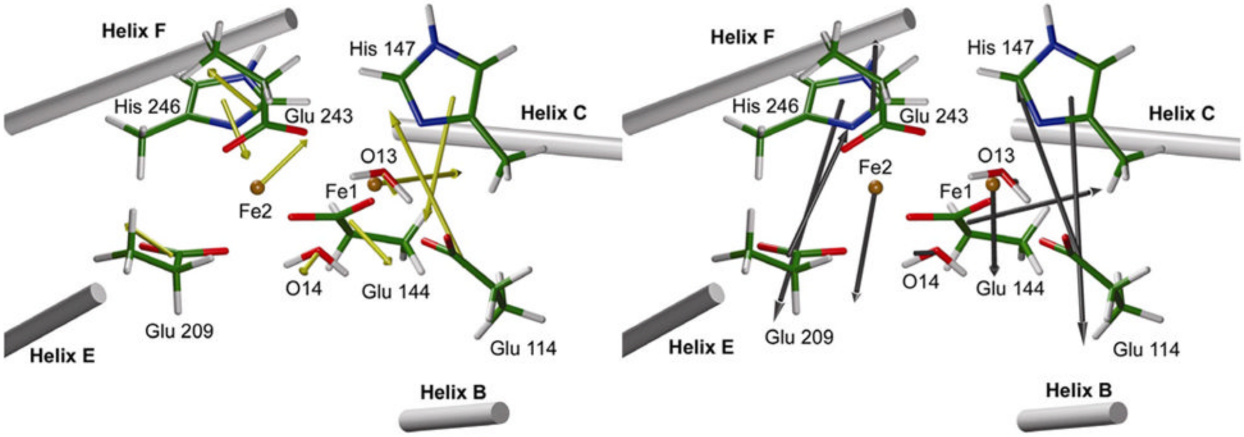

Figure 5.

Forces of the protein acting on the QM residues of the active site. On the left, forces correspond to the entire forces (QM forces calculation carried out in vacuum). On the right, forces correspond to what we call “tension forces”, i.e. total forces minus the electrostatic forces of the protein (QM forces calculation with MM charge distribution of the protein included).

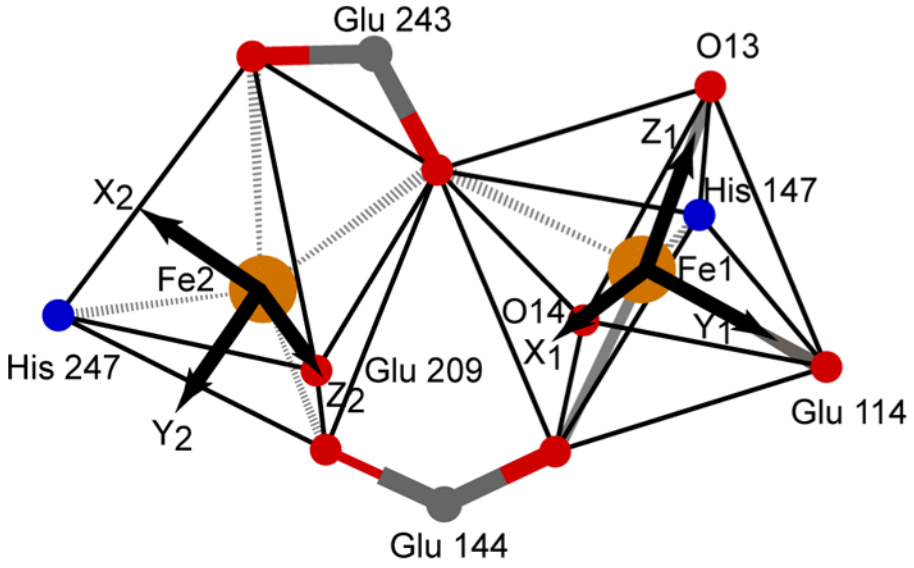

Figure 6.

Coordination geometries of the two iron atoms in the reduced state. Fe1 is in an octahedral environment, the axial direction of which is defined by the vector Glu 144-O13 (Z_1 vector). Fe2 is in a square pyramidal environment, the axial direction of which is defined by the Fe2-Glu 209 direction (Z_2 vector). Directions X1, Y1 and Z2 are oriented toward the front of the page.

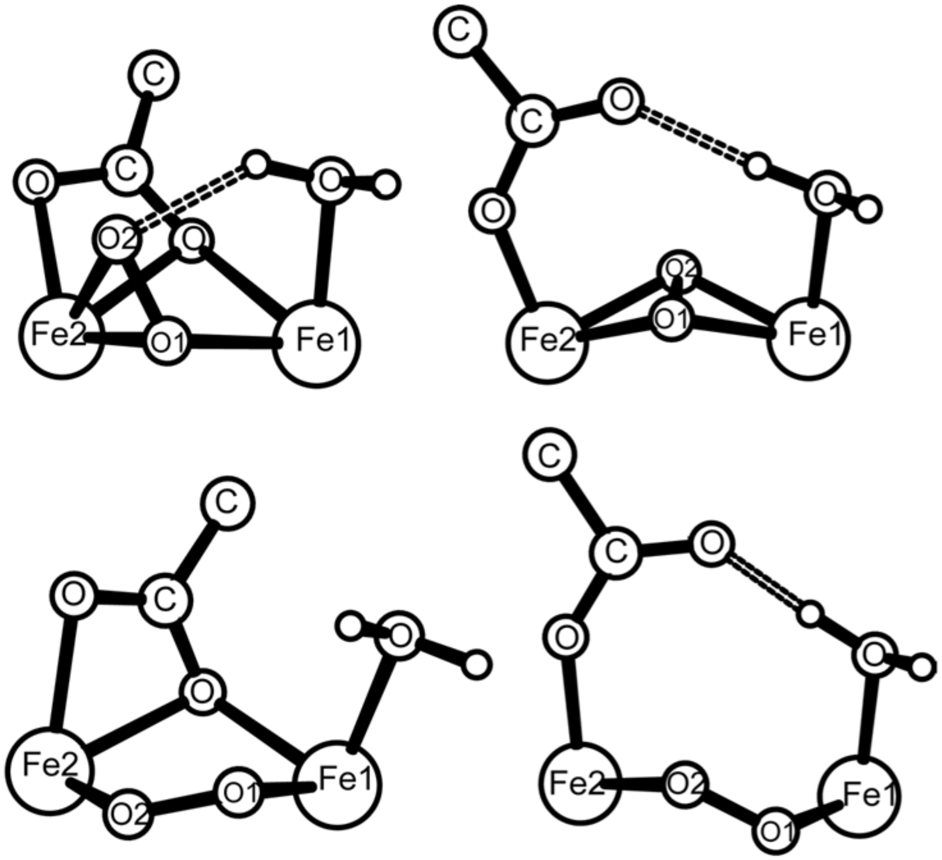

Figure 7.

Four tested geometries for H_{peroxo}. In the upper left, the structure is similar to $H_{superoxo}$ with a shifted Glu 243 and the peroxide coordinated to iron in a μ-η^2, η^1 fashion. In the upper right, the peroxide adopts a μ-η^2,η^2 butterfly arrangement. Both structures have been previously studied at the QM level. In the lower part, structures with peroxide coordinated to iron in a cis-μ-1,2 fashion are presented. On the left, the structure is similar to $H_{superoxo}$ with a shifted Glu 243 ($A\mu 12H_{peroxo}$), while on the right ($S\mu 12H_{peroxo}$) it is similar to the μ-η^2,η^2 butterfly peroxo arrangement with Glu 243 having the same conformation as in the crystal structure of the oxidized form.

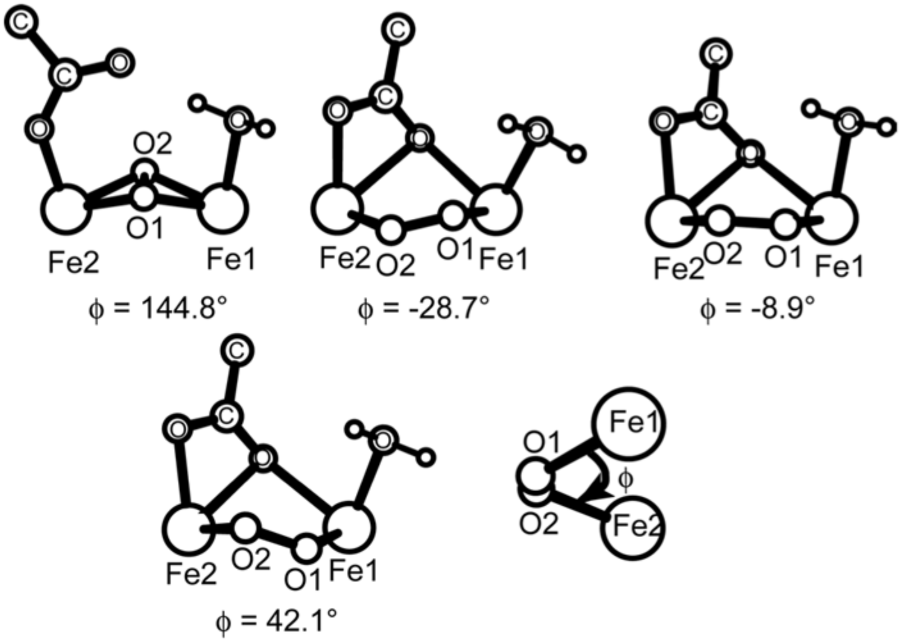

Figure 8.

Geometry of the μ-η^2,η^2 butterfly structure of H_{peroxo} and different conformers for the Aμ-1,2 H_{peroxo} structure. The dihedral angle between iron atoms and the peroxide moiety (φ) is also defined (Fe1-O1-O2-Fe2). The first gauche conformation (top left) has a negative angle close to −30 and the second conformer has a positive one close to 40. These two conformers have similar energies and have similar structures as those found in cis-μ-1,2-peroxo model compounds.[26] The last conformer (top right) is closer to the structures found in other cis-μ-1,2-peroxo model compounds.[91, 92]

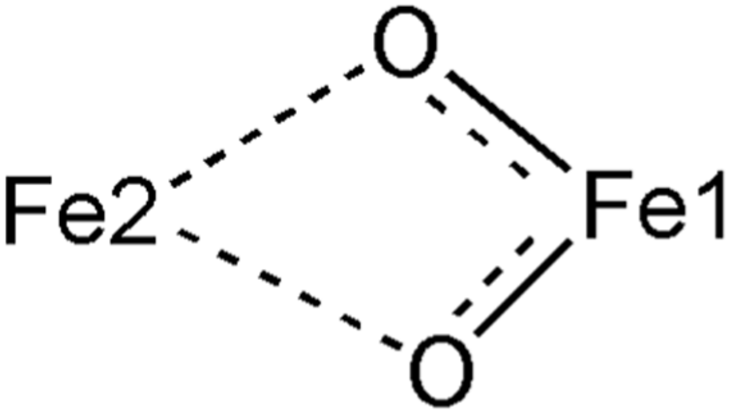

Figure 9.
Asymmetric structure for H_Q derived from QM/MM calculations.

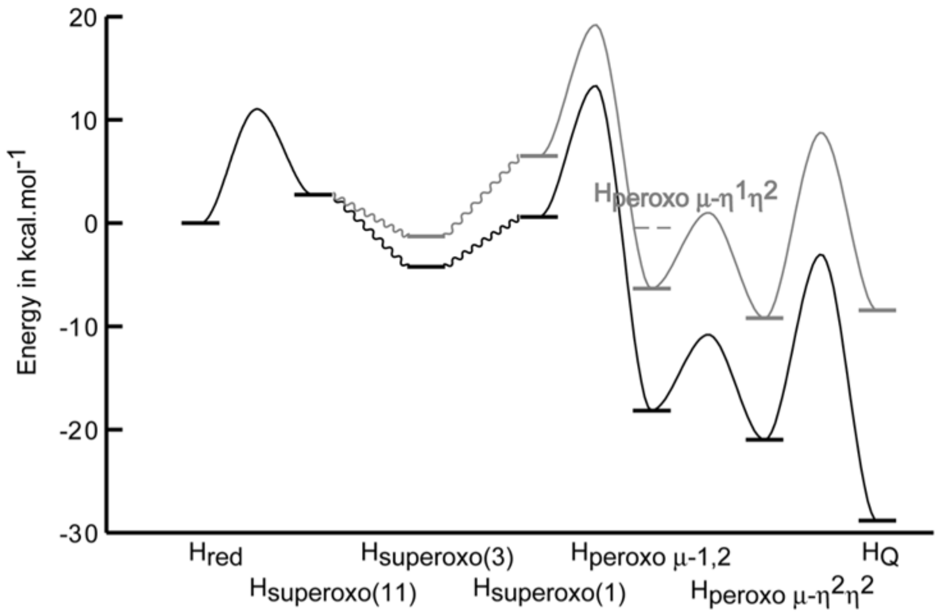

Figure 10.

Schematic reaction energy profile of the QM/MM intermediates as found with B3LYP (gray) and B3LYP-LOC (black).

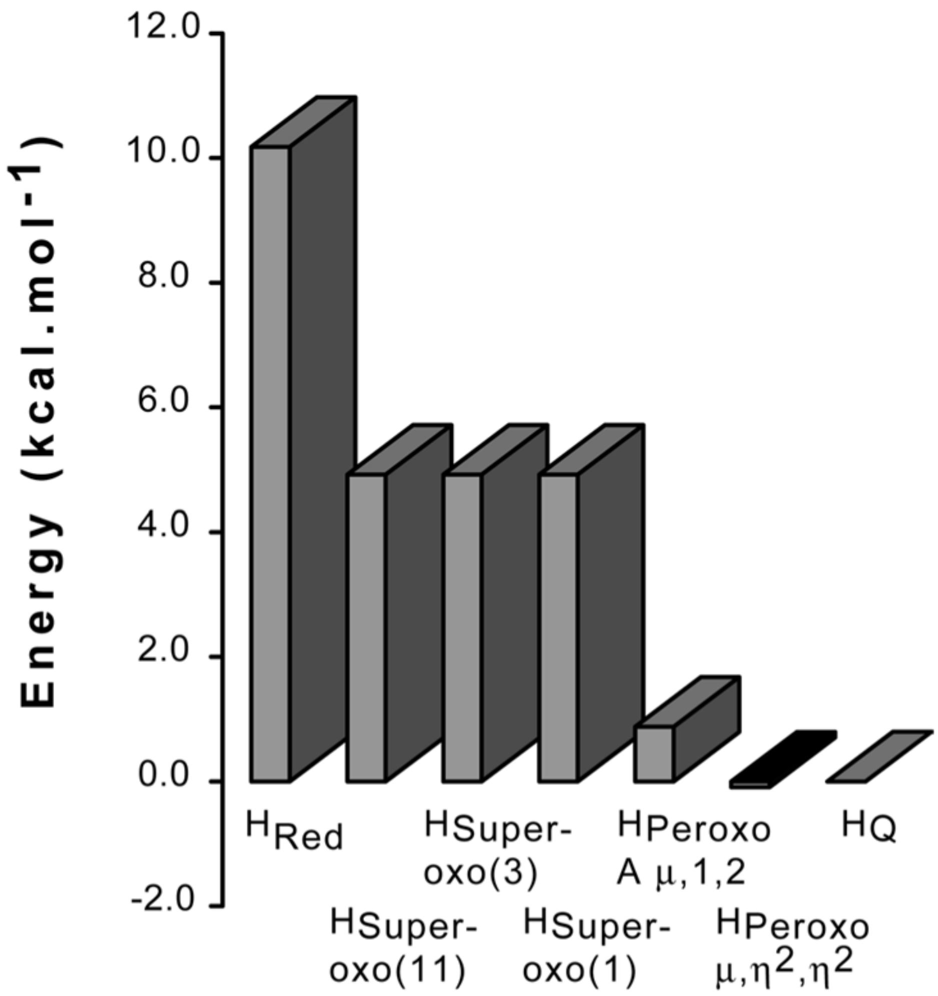

Figure 11.

Destabilization energies (in kcal/mol) due to the protein matrix computed from our QM/MM//RDFT models ($\Delta[E_{QM/MM} - E_{QM\text{-}RODFT}]$ with H_Q taken as a reference in Table S-4 and discussion on the QM/MM//UDFT and QM/MM//RDFT in Supporting Information). The protein matrix effects destabilize more intermediates closer to the reduced form in the reaction pathway.

$$CH_4 + NADH + H^+ + O_2 \longrightarrow CH_3OH + H_2O + NAD^+$$

Scheme 1.

Table 1

Selected distances between irons and atoms in their first coordination sphere for our QM/MM model of the reduced form: $MMOH_{red}$ and the experimental structure.[a]

Distance (Å)	Model QM/MM	Model QM	Crystal protomer β	Deviation QMMM/Protomer β	Deviation QM/Protomer β	Deviation QMMM/QM	Deviation Protomer β/Protomer α
Fe2-Fe1	3.289	3.636	3.267	0.022	0.369	−0.347	−0.046
O3-Fe1	2.047	2.120	2.064	−0.017	0.056	−0.073	−0.069
O5-Fe1	2.039	2.066	2.283	−0.244	−0.217	−0.027	0.051
N7-Fe1	2.158	2.219	2.196	−0.038	0.023	−0.061	−0.083
O11-Fe1	2.475	2.246	2.315	0.160	−0.069	0.229	−0.126
O13-Fe1	2.109	2.140	2.184	−0.075	−0.044	−0.031	−0.301
O14-Fe1	2.312	2.346	2.528	−0.216	−0.182	−0.034	0.148
O6-Fe2	2.097	2.098	2.295	−0.198	−0.197	−0.001	0.015
O8-Fe2	1.950	1.964	2.070	−0.120	−0.106	−0.014	0.073
O10-Fe2	2.220	2.292	2.366	−0.146	−0.074	−0.072	−0.071
O11-Fe2	2.265	2.163	2.262	0.003	−0.099	0.102	−0.188
N12-Fe2	2.110	2.148	2.162	−0.052	−0.014	−0.038	−0.008
O14-Fe2	2.910	3.201	2.654	0.256	0.547	−0.291	−0.022
RMSD (A)				0.147	0.213	0.148	0.121

---

[a] Experimental results are from structure PDB1FYZ[87] and atom numbering is shown in Figure 3.

Table 2

Norms of the resultant of forces exerted by the protein on each residue of the active site in our QM/MM//RDFT model of the reduced form.[b]

Residues	Total force in mHartree/Bohr	"Tension" force in mHartree/Bohr
Glu 114	16.24	18.59
Glu 144	6.76	15.14
His 147	11.66	22.56
Glu 209	6.74	12.71
Glu 243	9.11	7.76
His 246	9.84	23.79
Fe1	13.16	10.39
Fe2	6.29	11.61
O13	2.74	3.17
14	3.27	2.48

---

[b] Results are given in mHartree/Bohr for the whole forces and for its non-electrostatic component ("tension force").

Table 3

Iron-Iron distances (in Å) for intermediates as calculated with QM/MM models and with big models at the pure QM level.[19c]

Species	$S_z(S_z+1)$	QMM/MM	QM	Difference
H_{red}	9	3.29	3.64	0.35
$H_{red-no-wat}$	9	3.38	3.76	0.38
$H_{superoxo}$	11	3.44	3.79	0.35
$H_{superoxo}$	3	3.41	3.65	0.24
$H_{superoxo}$	1	3.46	3.51	0.05
H_{peroxo} (μ-η 2,η 2)	1	3.48	3.61	0.13
H_{peroxo} (μ-η 2,η 1)	1	3.27	3.36	0.09
H_{peroxo} (Aμ12)*	1	3.47	3.57	0.10
H_{peroxo} (Sμ12)*	1	3.64	4.02	0.38
H_Q*	1	2.84	2.70	−0.14

---

[c] Results marked by a star were obtained with a medium model for pure QM calculations. The difference between the two models is also shown

Table 4

Summary of the frequencies for the ν(O-O) and ν(Fe-O) modes obtained from our theoretical models of A- μ1,2 H_{peroxo} and μ, η^2, η^2 H_{peroxo}.[d]

	ν (^{16}O-^{16}O) (cm^{-1})	**Δ [^{18} O_2] (cm^{-1})**	**ν (Fe-^{16}O) (cm^{-1})**	**Δ [$^{18}O_2$] (cm^{-1})**
A-μ1,2 H_{peroxo}	1004 (975)	48	441 (429)	20
Fe_2 (μ-O_2)[(μ-O_2CPh)]$_2$ [HB(pz′)$_3$]$_2$[26]	888	46	415	11
μ, η^2, η^2, H_{peroxo}	815 (823)	43.8	544 (473)	15.4

---

[d] The experimental values coming from a model compound of A-μ1,2 H_{peroxo} are also presented. In brackets, the unscaled frequencies calculated with a high-level basis set on the diiron-core (LACV3P** for Fe, cc-pVTZ(-f)++ for dioxygen) and using a QM/MM model optimized at the same level are given.

Table 5

Detailed breakdown of the QM/MM//UDFT free energies (at 298 K) relative to the reduced state of putative intermediates for the activation of dioxygen reaction proposed based on QM/MM//RDFT results.[e]

Model	$\mathbf{H_{Red}}$	$\mathbf{H_{Superoxo}}$ **(11)**	$\mathbf{H_{Superoxo}}$ **(3)**	$\mathbf{H_{Superoxo}}$ **(1)**	$\mathbf{H_{Peroxo}}$ **Aμ-1,2 (1)**	$\mathbf{H_{Peroxo}}$ $\boldsymbol{\mu,\eta^2,\eta^1}$ **(1)**	$\mathbf{H_{Peroxo}}$ $\boldsymbol{\mu,\eta^2,\eta^2}$ **(1)**	$\mathbf{H_Q}$ **(1)**
$\Delta E_{QM/MM\text{-}UDFT}$	0	4.64	1.72	5.65	−3.40	−6.28	−9.27	−8.86
ΔZPE	0	−3.5	−3.66	−2.71	−3.38	2.95	−2.75	−2.37
$\Delta\Delta H_{Corrections}$	0	0.21	0.81	−0.09	1.17	0.23	−0.22	−0.22
ΔS	0	−4.68	0.54	−12.21	2.26	−8.98	−13.25	−16.02
−TΔS	0	1.39	−0.16	3.64	−0.67	2.68	3.95	4.78
Spin-projection Corrections	-	-	-	-	−0.08	−0.04	−0.90	−1.76
ΔH	0	1.35	−1.13	2.85	−5.69	−3.14	−13.14	−13.21
ΔG	0	2.74	−1.29	6.49	−6.36	−0.46	−9.19	−8.43

---

[e] All energies are given in kcal/mol except ΔS which is given in cal/mol·K. Multiplicity of the state studied is written in brackets. ZPE, entropy and enthalpy corrections are based on pure QM frequency calculations.

Table 6

Heisenberg exchange coupling constants (J) and corrections to the BS energies induced by spin projection for the QM/MM model.

Species	**$S_z(S_z+1)$**	**J (cm^{-1})**	**ΔE (kcal/mol)**
H_{Red}	9	−25	−0.29
$H_{Red\text{-}no\text{-}wat}$	9	23	0.26
H_{Peroxo} A (μ-1,2)	11	−6	−0.08
H_{peroxo} (μ-η^2,η^1)	11	−2	−0.04
H_{peroxo} (μ-η^2,η^2)	11	−63	−0.90
H_Q	9	−154	−1.76

Table 7

Detailed breakdown of the B3LYP-LOC calculation based on the B3LYP free energies obtained using a big basis set with diffuse functions on atoms of dioxygen.[f]

Model	H_{Red}	$H_{Superoxo}$ (11)	$H_{Superoxo}$ (3) (red)	$H_{Superoxo}$ (3) (1/2,1/2)	$H_{Superoxo}$ (3) (superoxo)	$H_{Superoxo}$ (1)	H_{Peroxo} Aμ-1,2 (1)	H_{Peroxo} $\mu\eta^2,\eta^2$(1)	H_Q (1)
ΔG(B3LYP)	0	2.74	−1.29	−1.29	−1.29	6.49	−6.36	−9.19	−8.43
AT	2×1.0	2×1.0	2×1.0	1.0+1.4	1.0+1.8	1.0+1.8	2×1.8	2×1.8	2×1.0
BOND	−1.0	−1.0	−1.0	−0.5+-0.75	−0.5+-1.0	−0.5+-1.0	−2.0	−2.0	0.0
EBSC	0.0	0.0	0.0	0.0	0.0	0.0	0.0	0.0	0.0
RAD	2×1.7	2×1.7	2×1.7	1.7+0.85	1.7	1.7	0.0	0.0	0.0
CT	0.0	0.0	0.0	−2.25	−4.5	−4.5	2×−4.5	2×−4.5	4×−4.5
TOT Corrections	4.4	4.4	4.4	1.45	−1.5	−1.5	−7.4	−7.4	−16
ΔG(B3LYP-LOC)	0	2.74	−1.29	−4.24	−7.19	0.59	−18.16	−20.99	−28.83

---

[f] For $H_{superoxo(3)}$, three types of corrections were applied depending if the valence structure of this species was considered to be closer to the reduced state ($H_{superoxo(3)}$ (red)), to the true superoxo state ($H_{superoxo(3)}$ (superoxo)) or just in between, thus requiring half corrections from $H_{reduced}$ and half corrections from $H_{superoxo(1)}$ ($H_{superoxo(3)}$ (1/2,1/2)).